

Magnetic Flux of Active Regions Determining the Eruptive Character of Large Solar Flares

Ting Li^{1,2}, Yijun Hou^{1,2}, Shuhong Yang^{1,2}, Jun Zhang^{3,1}, Lijuan Liu^{4,5} & Astrid M. Veronig⁶

ABSTRACT

We establish the largest eruptive/confined flare database to date and analyze 322 flares of *GOES* class M1.0 and larger that occurred during 2010–2019, i.e., almost spanning the entire solar cycle 24. We find that the total unsigned magnetic flux (Φ_{AR}) of active regions (ARs) is a key parameter in governing the eruptive character of large flares, with the proportion of eruptive flares exhibiting a strong anti-correlation with Φ_{AR} . This means that an AR containing a large magnetic flux has a lower probability for the large flares it produces to be associated with a coronal mass ejection (CME). This finding is supported by the high positive correlation we obtained between the critical decay index height and Φ_{AR} , implying that ARs with a larger Φ_{AR} have a stronger magnetic confinement. Moreover, the confined flares originating from ARs larger than 1.0×10^{23} Mx have several characteristics in common: stable filament, slipping magnetic reconnection and strongly sheared post-flare loops. Our findings reveal new relations between the magnetic flux of ARs and the occurrence of CMEs in association with large flares. These relations obtained here provide quantitative criteria for forecasting CMEs and adverse space weather, and have also important implications for “superflares” on solar-type stars and stellar CMEs. The link of database <https://doi.org/10.12149/101030>

¹CAS Key Laboratory of Solar Activity, National Astronomical Observatories, Chinese Academy of Sciences, Beijing 100101, China; liting@nao.cas.cn

²School of Astronomy and Space Science, University of Chinese Academy of Sciences, Beijing 100049, China

³School of Physics and Materials Science, Anhui University, Hefei 230601, China

⁴School of Atmospheric Sciences, Sun Yat-sen University, Zhuhai, Guangdong, 519082, China

⁵CAS Center for Excellence in Comparative Planetology, China

⁶Institute of Physics & Kanzelhöhe Observatory for Solar and Environmental Research, University of Graz, A-8010 Graz, Austria

Subject headings: Sun: activity—Sun: coronal mass ejections (CMEs)—Sun: flares—Sun: magnetic fields

1. Introduction

Solar flares and coronal mass ejections (CMEs) are the most energetic phenomena in our solar system and are the dominant contributors to adverse space weather at Earth (Gosling et al. 1991; Green et al. 2018). They originate from the rapid release of free magnetic energy stored in the sheared or twisted magnetic fields of active regions (ARs) through magnetic reconnection (Forbes 2000; Shibata & Magara 2011). Magnetic reconnection is believed to be a fundamental process in magnetized plasma systems throughout the Universe where magnetic energy is stored over relatively long times to be released suddenly in bursts of various forms (thermal, kinetic, and high-energy particle) (Priest & Forbes 2000; Su et al. 2013). Flares associated with a CME are usually referred to as eruptive events, while flares that are not accompanied by a CME are called confined or “CME-less” events (Svestka 1986; Moore et al. 2001). The association rate of flares and CMEs has revealed that most small flares occur without a CME, whereas for large flares (M-class, X-class) the CME-association is steeply increasing, and reaches 100% for the biggest events (Andrews 2003; Yashiro et al. 2006). The broad variety of strong space weather effects is mostly due to the CME rather than the flare itself. Our understanding of the physical mechanism of flares and their relationship with CMEs is important to forecast space weather in the near-Earth environment (Forbes 2000; Shibata & Magara 2011). Meanwhile, the solar flare-CME paradigm might be applied to magnetic activities in other stars, which is vital for the question of exoplanet habitability and the evolution of stellar mass loss and rotation (Khodachenko et al. 2007; Lammer et al. 2007).

Substantial observational studies have revealed that a flare would be confined if the strapping magnetic field overlying the flaring region is too strong or does not decrease sufficiently fast with height (Green et al. 2002; Wang & Zhang 2007; Cheng et al. 2011; Yang et al. 2014; Chen et al. 2015; Thalmann et al. 2015). To quantify the decline of the strapping field with height, the decay index has been used (Kliem & Török 2006; Fan & Gibson 2007; Zuccarello et al. 2015), i.e., $n = -d \ln B_{hor} / d \ln h$, with B_{hor} denoting the horizontal field and h the height in the corona. The torus instability of a magnetic flux rope occurs when the decay index n reaches a critical value $n_{crit} \approx 1.5$ (Kliem & Török 2006; Fan & Gibson 2007). Recent magnetohydrodynamics (MHD) simulations showed that the overlying field lines form a confining cage and a weaker magnetic cage would produce a more energetic eruption with

a CME (Amari et al. 2018). Another important factor that governs the eruptive character of solar flares is the non-potentiality of ARs. Statistical studies have shown that flare and CME productivity are correlated with magnetic shear, electric current, magnetic free energy, etc (Hagyard & Rabin 1986; Falconer et al. 2002; Liu et al. 2016a). It is suggested that AR eruptivity is related to the relative value of magnetic non-potentiality over the restriction of the background field (Sun et al. 2015).

In this paper, we derive important quantitative relations between the magnetic properties of ARs and the eruptive character of large solar flares, based on the *Solar Dynamics Observatory* (*SDO*; Pesnell et al. 2012) observations during the period of solar cycle 24. A total of 322 flares (170 eruptive and 152 confined) of Geostationary Operational Environmental Satellite (*GOES*) class M1.0 and larger that occurred within 45° from the central meridian, from June 2010 until June 2019, are selected. About 51% (155 of 301) of the M-class flares are eruptive and the percentage increases up to $\sim 71\%$ (15 of 21) for X-class flares, similar to the previous results (Yashiro et al. 2006). To our knowledge, the eruptive/confined flare sample established in this study is by far the largest one in the era of *SDO*. We show that total unsigned magnetic flux of ARs (Φ_{AR}) is a decisive parameter in governing the eruptive character of flares, and the proportion of eruptive flares exhibits a strong anti-correlation with Φ_{AR} . This finding is further supported by the high correlation obtained between Φ_{AR} and the critical height for torus instability.

The rest of the paper is organized as follows. In Sections 2 and 3, we describe the data analysis and show the statistical results, respectively. Section 4 presents the detailed analysis for six events as typical examples. Finally, we summarize our findings and discuss the implications in Section 5.

2. Data Analysis

2.1. Event Sample

The *SDO* satellite has already provided a rich database since its launch in February 2010. Until now, its observation period lasts about 10 years and almost spans the entire solar cycle 24. Thus it is a good opportunity to carry out statistical analysis about the flare-CME mechanism based on the *SDO* observations. Firstly, we examined a database RibbonDB presented by Kazachenko et al. (2017) and selected all 302 flare events larger than M1.0 that occurred within 45° from the central meridian, from June 2010 until April 2016. To extend the time period, we checked for the *GOES* soft X-ray (SXR) flare catalog to search for flare events from May 2016 to June 2019 and found 20 flares of *GOES* class M1.0 and

greater. A total of 322 flare events are involved in our database over a nine-year period (see Table FlareM1.0). Secondly, for each flare, its CME association was determined by checking the CME catalog¹ (Gopalswamy et al. 2009) of the Solar and Heliospheric Observatory (SOHO)/Large Angle and Spectrometric Coronagraph (LASCO). We regarded a flare as eruptive if the CME onset time was within 90 min of the flare start time and the position angle of the CME agreed with the quadrant on the Sun where the flare occurred. Moreover, we also inspected the observations of the *twin Solar Terrestrial Relations Observatory (STEREO)* (Kaiser et al. 2008; Howard et al. 2008) to check from a different viewing angle if there is an associated CME. For the events difficult to determine the classification, e.g., there are two flares within a short time or the CME is too weak to be identified, we then checked the EUV observations from the Atmospheric Imaging Assembly (AIA; Lemen et al. 2012) on board the *SDO* and identified the coronal EUV wave manually. If a global coronal EUV wave was associated with the flare, the flare was classified as eruptive. Out of these 322 flares, 170 ($\sim 53\%$) events were eruptive (155 M- and 15 X-) and 152 ($\sim 47\%$) were confined (146 M- and 6 X-).

2.2. Data and Methods

We investigated the relations between the AR parameters (unsigned AR magnetic flux Φ_{AR} and AR area) and the eruptive character of large solar flares. The AR parameters in RibbonDB catalog (Kazachenko et al. 2017) are calculated based on the full-disk Helioseismic and Magnetic Imager (HMI; Scherrer et al. 2012) vector magnetogram data series (`hmi.B_720s`) before the flare onset time. To avoid noisy magnetic fields, only pixels that host a normal component of the magnetic field $|B_n| > 100$ G are considered. For the flare events that are not included in the RibbonDB catalog, we use the available vector magnetograms (`hmi.sharp_cea_720s`) from Space-Weather HMI AR Patches (Bobra et al. 2014) before the flare onset. The magnetograms were re-mapped using a cylindrical equal area projection with a pixel size of $\sim 0''.5$ and presented as (B_r, B_θ, B_ϕ) in heliocentric spherical coordinates corresponding to $(B_z, -B_y, B_x)$ in heliographic coordinates (Sun 2013). Similarly, to calculate the AR magnetic flux and AR area, we consider all pixels of $|B_r| > 100$ G. Moreover, RibbonDB catalog (Kazachenko et al. 2017) also includes the parameters of flare ribbons such as the flare ribbon reconnection flux Φ_{ribbon} , the cumulative flare ribbon area S_{ribbon} , the ratio of the AR magnetic flux involved in the flare reconnection R_{flux} (Φ_{ribbon}/Φ_{AR}) and the area ratio R_S (S_{ribbon}/S_{AR}). In this work, we also use these parameters of 302 flare events larger than M1.0 and investigate their distributions and correlations in

¹https://cdaw.gsfc.nasa.gov/CME_list/

eruptive and confined flares.

The role of the background coronal fields in confined and eruptive flares was estimated by calculating the decay index n above the ARs. In order to extrapolate the 3D magnetic field in the entire AR volume, we use the Fourier transformation method (Alissandrakis 1981) to extrapolate the potential field. The method yields the local potential field with a resolution around 0.72 Mm, same as the resolution of the boundary condition. The boundary condition is the normal component of the photospheric magnetic field from Space-Weather HMI AR Patches (Bobra et al. 2014) observed prior to the flare start. From the extrapolated field, the mean value of the horizontal magnetic field, $\langle B_{hor} \rangle$, as a function of height is obtained along the main polarity inversion line (PIL) and an average decay index, $\langle n \rangle$, is then derived. Here, the main PIL was identified as zero Gauss contour in the bottom vertical magnetic field (B_r) image from the extrapolated potential fields (Bokenkamp 2007; Vasantharaju et al. 2018). To analyze the structure and dynamics of typical flare examples, we used the E(UV) observations from the AIA, with a resolution of $\sim 0''.6$ per pixel and a cadence of 12(24) s. Five channels of AIA 1600, 304, 171, 94 and 131 Å were mainly applied to analyze the appearances of the flares. The full-disk line-of-sight (LOS) magnetic field data from the HMI are also used to present the ARs producing the typical flare examples.

3. Statistical Results

3.1. Magnetic Properties of ARs and Eruptive Character of Solar Flares

Figure 1(a) shows the scatter plot of the flare peak X-ray flux versus Φ_{AR} . Blue (red) circles are the eruptive (confined) flares. Obviously, when Φ_{AR} is small enough, the flares tend to be eruptive (Area A in Figure 1(a)). About 92% (36 of 39) of events occurring in ARs with Φ_{AR} smaller than 3.0×10^{22} Mx are eruptive. An overwhelming majority of flares that are hosted by ARs with a large magnetic flux do not generate CMEs (Area C in Figure 1(a)). The proportion of confined flares of GOES class $\geq M1$ is $\sim 93\%$ (26 of 28) corresponding to the AR with Φ_{AR} larger than 1.0×10^{23} Mx. We examined two special eruptive events (M4.0-class flare on 24 October 2014 in Figure 10 and X1.8-class event on 20 December 2014) in Area C of Figure 1(a) and found that they either were located at the edge of the AR or caused a sympathetic eruption of a nearby quiescent filament. If the AR has a moderate magnetic flux (larger than 3.0×10^{22} Mx and smaller than 1.0×10^{23} Mx), the likelihood of eruptive and confined events appears to be almost equal (132 eruptive flares and 126 confined events of 258 in Area B of Figure 1(a)). The scatter plot of the flare peak X-ray flux versus total AR area shows a similar trend (Figure 1(b)). All flares in ARs with an area smaller than $5.0 \times 10^{19} \text{ cm}^2$ are eruptive (Area A in Figure 1(b)) and all flares in ARs

larger than $3.0 \times 10^{20} \text{ cm}^2$ are confined (Area C in Figure 1(b)).

Figures 1(c)-(d) display the histograms for confined and eruptive events. There are significant differences in distributions of AR magnetic flux and AR area between the confined and eruptive cases. The confined events have larger AR magnetic flux and AR area. The averages of the log values of Φ_{AR} (indicated by vertical dotted lines) are $6.3 \times 10^{22} \text{ Mx}$ and $4.4 \times 10^{22} \text{ Mx}$ for confined and eruptive cases, respectively. The log-mean values of AR area for the confined and eruptive events are $1.5 \times 10^{20} \text{ cm}^2$ and $1.2 \times 10^{20} \text{ cm}^2$, respectively. Based on the the number distributions of AR magnetic flux and AR area between the confined and eruptive cases, we display the relations of the proportions of eruptive flares P_E ($P_E = N_E / (N_E + N_C)$, N_E and N_C are numbers of eruptive and confined events, respectively) with Φ_{AR} and AR area in Figures 1(e)-(f). It can be seen that P_E decreases with Φ_{AR} . The proportion P_E has a strong anti-correlation with Φ_{AR} at the Spearman rank order correlation coefficient r_s of -0.97 . The Spearman rank correlation provides a measure of the monotonic relationship between two variables. The linear fitting to the scatter plot provides the relation of

$$P_E = (-0.75 \pm 0.06) \log |\Phi_{AR}| + (17.53 \pm 1.27), \quad (1)$$

where Φ_{AR} is in units of [Mx].

Similarly, the proportion P_E shows a strong anti-correlation with AR area ($r_s = -0.95$), and provides the relation of

$$P_E = (-0.76 \pm 0.09) \log S_{AR} + (15.70 \pm 1.86), \quad (2)$$

where S_{AR} is in units of [cm^2].

3.2. Role of the Background Coronal Fields

We investigate the role of the background coronal fields by calculating the decay index n above the ARs. Figure 2 shows four examples including one eruptive flare in Area A of Figure 1(a) and three confined flares in Area C of Figure 1(a). Black asterisks denote the $\langle B_{hor} \rangle$ versus h profiles and blue diamonds are the $\langle n \rangle$ versus h profiles. The error bars mark the corresponding standard deviation. The critical height for torus instability h_{crit} corresponds to the height where $\langle n \rangle$ reaches a value of 1.5 (Kliem & Török 2006; Fan & Gibson 2007). Clearly, the h_{crit} value of AR 11305 ($\sim 17 \text{ Mm}$) with a small magnetic flux is lower than those of three other ARs (36–60 Mm) with larger magnetic fluxes, which means that the constraining field above AR 11305 producing an eruptive flare decays more rapidly than other ARs with confined flares, and therefore a perturbation in the lower corona may

cause the CME seed to erupt out more easily (Wang & Zhang 2007; Liu et al. 2018).

Following the procedure described above, we estimated the critical decay index heights h_{crit} for 82 events (including all the events in Areas A and C of Figure 1(a) and 15 flares in Area B of Figure 1(a)). Figure 3(a) shows the scatter plot of h_{crit} versus Φ_{AR} . It can be seen that h_{crit} increases with Φ_{AR} . This indicates that ARs with a larger magnetic flux tend to have stronger constraining field. The critical decay index height has a strong correlation with AR magnetic flux at the Spearman rank order correlation coefficient r_s of 0.86. The linear fitting to the scatter plot provides the relation of

$$h_{crit}=(38.31\pm 2.37)\log|\Phi_{AR}|+(-834.53\pm 53.92), \quad (3)$$

where h_{crit} and Φ_{AR} are in units of [Mm] and [Mx], respectively.

Using this equation, an Φ_{AR} value of 3.0×10^{22} Mx yields a h_{crit} of ~ 27 Mm (left vertical and bottom horizontal lines in Figure 3(a)) and 1.0×10^{23} Mx corresponds to h_{crit} of about 47 Mm (right vertical and top horizontal lines in Figure 3(a)). In Figure 3(b), we plot the flare peak X-ray flux versus h_{crit} . All flares $\geq M1$ (28 events) with a h_{crit} value smaller than 27 Mm are eruptive (Area A in Figure 3(b)), and about 95% (20 of 21) of events with h_{crit} larger than 47 Mm are confined (Area C in Figure 3(b)). The results of Figures 1 and 3 suggest that stronger strapping fields over the ARs with a larger magnetic flux play the major role in confining the eruption.

3.3. Relations of Flare Reconnection Flux with Flare Peak X-Ray Flux

Figure 4 shows the scatter plots of flare ribbon reconnection flux and cumulative flare ribbon area versus flare peak X-ray flux. We find that flare reconnection flux Φ_{ribbon} correlates with flare peak X-ray flux F_{SXR} at a moderate rank order correlation coefficient r_s of 0.51 for all the flares (Figure 4(a)). By fitting the data, we obtained their empirical relationship

$$\log|\Phi_{ribbon}|=(0.51\pm 0.04)\log F_{SXR}+(24.02\pm 0.17), \quad (4)$$

where Φ_{ribbon} and F_{SXR} are in units of [Mx] and [W/m^2], respectively.

The rank order correlation coefficient r_s for the subset of eruptive flares ($r_s=0.58$) is larger than r_s for the confined flares ($r_s=0.42$). The corresponding fitting parameters for the subsets of confined and eruptive flares show no significant differences.

The ribbon area and flare peak X-ray flux (Figure 4(b)) also show a moderate correlation with a rank order correlation coefficient r_s of 0.58 and their relation is

$$\log S_{ribbon}=(0.49\pm 0.03)\log F_{SXR}+(21.12\pm 0.14), \quad (5)$$

where S_{ribbon} and F_{SXR} are in units of $[cm^2]$ and $[W/m^2]$, respectively.

Similarly, there are no significant differences in the fitting parameters when considering confined and eruptive flares separately.

3.4. Flare Reconnection Flux Ratio and Area Ratio in Confined and Eruptive Flares

In Figures 5(a)-(b), we display the histograms of flare reconnection flux ratio R_{flux} (Φ_{ribbon}/Φ_{AR}) and ribbon area ratio R_S (S_{ribbon}/S_{AR}) for confined and eruptive events. It can be seen that the distributions of both R_{flux} and R_S show evident differences, with R_{flux} and R_S for confined events smaller than those for eruptive flares. R_{flux} ranges between 1% and 41% for eruptive flares and ranges between 1% and 21% for confined events. The proportion of eruptive flares reaches $\sim 89\%$ (39 of 44) corresponding to the flux ratio R_{flux} higher than 15%. The log averages of flux ratio R_{flux} are 6.3% for confined and 9.5% for eruptive events. Similarly, the confined flares have the smaller area ratio R_S (1%–18%) than eruptive events (1%–30%). The log-mean values of area ratio R_S are 4.0% for confined and 6.1% for eruptive cases.

4. Appearances of Typical Flare Examples

4.1. Two Confined Flares Within ARs of Large Magnetic Flux

We investigate the dynamic evolution of confined flares originating from ARs with a large magnetic flux ($\geq 1.0 \times 10^{23}$ Mx), including 26 events from 5 different ARs (ARs 11339, 11520, 11967, 12192 and 12242). After examining the AIA observations of these confined flares, we find that they have common characteristics: slipping reconnection, strong shear, and a stable filament. Here, two confined events from ARs 11520 and 12242 are taken as examples to analyze the flare dynamics and magnetic topological structures in detail.

On 10 July 2012, a confined M1.7 flare occurred in the sigmoidal region of AR 11520 with Φ_{AR} of 1.24×10^{23} Mx. The flare was initiated at 04:58 UT and the GOES SXR flux peaked at 05:14 UT. Before the flare started, a filament was located along the PIL at the flaring region (left panel in Figure 6(a)). It did not show any rise process during the flare and was stably present after the flare (right panel in Figure 6(a)). The comparison of the 304 Å image with the HMI LOS magnetogram showed that the flare consisted of two positive-polarity ribbons PR1-PR2 and two negative-polarity ribbons NR1-NR2 (middle panel in

Figure 6(a)). Ribbons PR1 and NR1 were located at two ends of the filament and PR2 and NR2 at both sides of the main body (axis) of the filament. High-temperature flare loops at 94 Å displayed notable dynamic evolution (Figure 6(b)). To display the fine structures of the EUV images, the 94 Å filter channel data have been processed using the multi-scale Gaussian normalization (MGN) method (Morgan & Druckmüller 2014). At the start of the flare, two sets of loop bundles L1 (connecting PR2-NR1) and L2 (connecting PR1-NR2) overlying the stable filament became bright. Starting from about 05:10 UT, a group of brightened short loops L3 were formed connecting PR2 and NR2, and meanwhile another longer loop bundles L4 linking PR1-NR1 can be discerned. During the flare, the north parts of loop bundles L2 and L3 exhibited apparent bidirectional slipping motions along ribbon NR2. Finally, strongly sheared post-flare loops (PFLs) appeared above the non-eruptive filament. Based on the dynamic evolution of flare loops and their relations with flare ribbons, we suggest that slipping magnetic reconnection (Priest & Démoulin 1995; Aulanier et al. 2006) between loop bundles L1 and L2 occurred and led to the formation of L3 and L4. We estimated the inclination angles θ of PFLs with respect to the PIL, corresponding to the angle between the tangents of the PFL and PIL at their intersection (left panel in Figure 6(c)). The complementary angle of θ has been referred to as the shear angle in previous studies (Su et al. 2007; Aulanier et al. 2012). We derive small θ values, ranging from 10° to 30° , indicative of a high non-potentiality in the form of a strong shear. Then more high-temperature PFLs gradually cooled down and formed PFLs overlying the stable filament at 171 Å (Figure 6(c)).

Using the photospheric vector magnetic field observed by SDO/HMI at 04:24 UT, we make a nonlinear force-free (NLFFF) extrapolation by applying the optimization method (Wheatland et al. 2000; Wiegelmann 2004) and obtain the 3D coronal magnetic fields. There are two sets of sheared magnetic systems (MS1 and MS2 in Figure 7(a)) overlying a twisted flux rope (FR) prior to the flare onset. By comparing the AIA observations with the extrapolation results, we suggest that the two magnetic systems MS1 and MS2 approximately correspond to two sets of loop bundles L1 and L2 (Figure 6(b)) and the flux rope FR bears a good resemblance to the observed non-eruptive filament (Figure 6(a)). Based on the extrapolated 3D coronal magnetic field, we calculated the squashing factor Q (Liu et al. 2016b) which defines the locations of the quasi-separatrix layers (QSLs) (Démoulin et al. 1996; Titov et al. 2002). As seen from the distribution of Q (Figure 7(b)), the observed flare ribbons are roughly matching the locations of high Q values, implying that magnetic reconnection involved in the flare probably occurs in regions of very strong magnetic connectivity gradients, i.e., QSLs.

Figure 8 shows another confined M1.3-class flare on 19 December 2014 in AR 12242, which has a large Φ_{AR} of $\sim 1.11 \times 10^{23}$ Mx. The flare was initiated at 09:31 UT and peaked at 09:44 UT. It occurred at the northwest of AR 12242 and a filament was present along

the PIL at the flaring region (Figure 8(a)). During the flare process, the mainbody of the filament did not show any rise phase except for the mild activation at its south part. After the flare, the filament remained stabilized, similar to the filament in the confined M1.7-class flare in AR 11520 (Figure 6(a)). Two quasi-parallel flare ribbons were distinguished from AIA 304 Å images, including ribbon PR in the leading positive-polarity sunspot and the negative-polarity ribbon NR. As shown from the high-temperature 131 Å observations, the flare loops were composed of two sets of magnetic systems S1 and S2 overlying the non-eruptive filament, displaying a clear “X-shape” structure (Figure 8(b)). The south ends of systems S1 and S2 were anchored in ribbon PR and their north ends in ribbon NR. During the flare evolution, S1 and S2 exhibited apparent slipping motions along ribbons PR and NR, and more flare loops successively appeared. In the gradual phase of the flare, low-temperature PFLs were formed as best observed in the AIA 171 Å channel (Figure 8(c)). Similarly, the early formed PFLs also displayed an “X-shape” structure. We estimated the inclination angles θ of PFLs with respect to the PIL and found θ values in the range of 20° – 28° . The small θ values imply that the PFLs are strongly sheared and have a higher non-potentiality.

The apparent slipping motions of the fine structures within flare ribbons are further displayed in Figure 9. Ribbon PR was composed of numerous bright dot-like substructures, corresponding to the footpoints of high-temperature flare loops. These substructures exhibited apparent slipping motions in opposite directions (Figure 9(a)). We followed the trails of 3 different substructures within ribbon PR. From 09:33:10 UT, the bright knot “1” slipped toward the east with a displacement of about 3.8 Mm in 110 s (with a velocity of ~ 30 km s^{-1}). Meanwhile, another bright knot “2” displayed a rapid slipping motion in the opposite direction at a velocity of ~ 130 km s^{-1} . At 09:34:58 UT, the bright knot “3” at the middle part of PR underwent a fast slippage towards the northeast. In order to analyze the slipping motions of the substructures, we create a stack plot (Figure 9(c)) along slice “C-D” in the AIA 131 Å images (blue curve in Figure 9(a)). As seen from the stack plot, the slipping motions along ribbon PR were in both directions with speeds of 20–150 km s^{-1} . Figure 9(b) shows the stack plot of the other ribbon NR along slice “A-B” (green dash-dotted curve in Figure 8(b)). Similarly, the slippage along ribbon NR was bi-directional with apparent speeds of 20–30 km s^{-1} , smaller than those of ribbon PR.

4.2. One Special Eruptive Event Within an AR of Large Magnetic Flux

A large majority of flares (26 of 28 events) originating from ARs of $\Phi_{AR} \geq 1.0 \times 10^{23}$ Mx are confined, however there are two special eruptive flares among the 28 events. One

event is M4.0 flare on 24 October 2014 and the other is X1.8 event on 20 December 2014. The X1.8 flare caused a sympathetic eruption of a nearby quiescent filament and generated a CME. Figure 10 displays the appearance of the eruptive M4.0 flare on 24 October 2014. The flare was initiated at 07:37 UT and peaked at 07:48 UT. It was located at the southeast of AR 12192, far away from the main PIL of the AR. The flare was triggered by a blow-out jet as seen in AIA 304 and 131 Å images, and produced a CME at 08:12 UT observed by LASCO/C2. It was suggested that the eruptive flare on the southern border of the AR was close to neighboring open field regions (Thalmann et al. 2015) and thus the jet successfully escaped from the solar surface and formed a CME.

4.3. One Eruptive Flare Within an AR of Small Magnetic Flux

About 92% events occurring in ARs with Φ_{AR} smaller than 3.0×10^{22} Mx are eruptive. Here, we present an eruptive M3.9 event on 02 October 2011 as an example (Figure 11). The flare originated from AR 11305 (N09°, W12°) with a smaller Φ_{AR} of $\sim 1.67 \times 10^{22}$. It started at 00:37 UT and reached its peak at 00:50 UT. A high-temperature flux rope erupted towards the southwest in 131 Å image. The angle of separation between *SDO* and *STEREO B* on 02 Oct 2011 was around 97°. An erupting CME bubble can be observed at the west limb in *STEREO B*/EUVI 195 Å image. Starting from about 01:05 UT, an Earth-directed CME was observed by the COR1 coronagraph aboard *STEREO B*.

4.4. One Eruptive and One Confined Flares Within the same AR of Medium Magnetic Flux

When Φ_{AR} is between 3.0×10^{22} and 1.0×10^{23} Mx, almost one half of flares are confined. Here, we show two examples from the same AR 11429 on 06 March 2012. At 07:52 UT, an eruptive M1.0-class flare occurred in AR 11429 with Φ_{AR} of about 6.78×10^{22} Mx measured before the flare onset (Figure 12). A reverse-S shaped filament was located along the PIL. During the flare, the middle part of the filament erupted and caused a CME. The AR was emerging persistently and the magnetic flux increased to $\sim 7.96 \times 10^{22}$ Mx at 12:00 UT. Then another confined M2.1-class flare occurred at 12:23 UT and peaked at 12:41 UT (Figure 13). The filament in the AR did not erupt except for the activation at the north part. A flux rope was illuminated and started to rise at 12:26 UT as observed in 131 Å images. The rise lasted for about 10 min and ceased at 12:37 UT. Then the flux rope seemed to stay at a certain height and faded away gradually. The eruption of the flux rope failed and did not generate any CME.

5. Summary and Discussion

In this work, we established the extensive database of eruptive/confined large flares in the *SDO* era (a total of 322 events including 170 eruptive and 152 confined cases). The morphological properties of flaring ARs and the flare ribbons, and their statistical relationships have been investigated. Our study delivered the following main results.

1. We find that the total unsigned magnetic flux Φ_{AR} of ARs plays an important role in governing the eruptive character of flares, and the proportion of eruptive flares exhibits a strong anti-correlation with Φ_{AR} ($r_s=-0.97$). About 93% flares originating from ARs with an unsigned magnetic flux larger than 1.0×10^{23} Mx are confined, i.e., are not associated with a CME. About 92% events occurring in ARs with Φ_{AR} smaller than 3.0×10^{22} Mx are eruptive.

2. We also find a very high positive correlation ($r_s=0.86$) empirical relation between critical decay index height h_{crit} and Φ_{AR} . This implies that ARs with a large magnetic flux have a strong magnetic cage, which confines the eruption. This is the first time that such a fundamental relation between the total AR flux and the confinement properties for large flares is derived.

3. We find that the flare ribbon reconnection flux and flare ribbon area are correlated with the peak X-ray flux. There are no significant differences in the fitting parameters when considering confined and eruptive flares separately. These findings are consistent with previous studies (Veronig & Polanec 2015; Kazachenko et al. 2017; Tschernitz et al. 2018), while the obtained correlation coefficients between flare reconnection flux Φ_{ribbon} and flare peak X-ray flux F_{SXR} are different, probably due to different ranges of flare classes in different statistical studies.

4. The ratio of the AR magnetic flux that is involved in the flare reconnection process ranges between 1% and 41% for eruptive flares and between 1% and 21% for confined events. Similarly, the confined flares have the smaller area ratio R_S (1%–18%) than eruptive events (1%–30%).

5. By analyzing the dynamic evolution of 26 confined flares occurring in ARs with $\Phi_{AR} \geq 1.0 \times 10^{23}$ Mx, we find that these flares have several characteristics in common: stable filament, slipping magnetic reconnection and strongly sheared PFLs, belonging to “type I” flares as proposed in our previous work (Li et al. 2019).

Our results show that the magnetic flux of ARs is a key parameter in determining the eruptive character of large solar flares, and the proportion of eruptive flares exhibits a strong anti-correlation with Φ_{AR} . The relation was first found in our work and has never been revealed before. This means that the association rate of flares and CMEs is decreasing

with the increasing magnetic flux of ARs. This finding is further supported by the high correlation obtained between Φ_{AR} and the critical height for torus instability. The ARs seem to be classified into three situations according to their different magnetic properties: strong confinement ($\Phi_{AR} \geq 1.0 \times 10^{23}$ Mx or $h_{crit} \geq 47$ Mm), moderate confinement ($3.0 \times 10^{22} < \Phi_{AR} < 1.0 \times 10^{23}$ Mx or $27 < h_{crit} < 47$ Mm) and weak confinement ($\Phi_{AR} \leq 3.0 \times 10^{22}$ Mx or $h_{crit} \leq 27$ Mm). The values we use to discriminate between classes, 3.0×10^{22} Mx and 1.0×10^{23} Mx, are arbitrary. In the case of strong confinement, the flare energy and associated magnetic reconfigurations are insufficient to break through the overlying field even if it is an X-class flare (e.g. AR 12192), thus tend to generate confined flares (Guo et al. 2010; Sarkar & Srivastava 2018; Jing et al. 2018; Duan et al. 2019). On the contrary, if the constraining effect of the background field is so small, small disturbance in the lower corona can result in the generation of a CME, which explains the high proportion of eruptive flares originating from ARs with a small magnetic flux. When the confinement of overlying magnetic cage is moderate, almost one half of flares are confined (Area B in Figure 1(a), also see two examples in Figures 12-13). This indicates that the overlying confinement and AR non-potentiality (Falconer et al. 2002; Nindos & Andrews 2004) may jointly determine the class of the flare in the moderate-confinement environment. Previous statistical studies have shown that confined flares are often located much closer to the AR centers where the strapping field is higher, whereas eruptive flares occur at the periphery of an AR (Wang & Zhang 2007; Baumgartner et al. 2018).

Moreover, it is also found that the flux ratio R_{flux} and area ratio R_S for confined flares are significantly smaller than those for eruptive events. This result is similar to the statistical result of Toriumi et al. (2017), who showed the parameter of the ribbon area normalized by the sunspot area determines whether a given flare is eruptive or not. They suggested that the relative structural relation between the flaring region and the entire AR controls the CME productivity.

Our findings reveal a new relation between the magnetic flux of ARs and the occurrence of CMEs in association with large flares. They also have important implications for stellar CMEs and the recently detected “superflares” on solar-type stars (Maehara et al. 2012; Lynch et al. 2019). In order to produce a large flare, the magnetic flux of the source AR has to be large (Aulanier et al. 2013; Shibata et al. 2013; Tschernitz et al. 2018). The historical observational data shows that the largest magnetic flux of flaring ARs is up to a few times 10^{23} Mx (Zhang et al. 2010; Chen et al. 2011; Schrijver et al. 2012). In the present study, between 1% and 41% of the magnetic flux of the source AR for eruptive flares and between 1% and 21% of Φ_{AR} for confined events are involved in the flare reconnection process. If we assume that the maximum percentage of 40% of the magnetic flux contained in the AR contributing to the flare reconnection process (Kazachenko et al. 2017; Tschernitz

et al. 2018), a total reconnection flux of $\sim 1.0 \times 10^{23}$ Mx can be obtained for an AR with Φ_{AR} of 2.3×10^{23} Mx (the maximum magnetic flux in our sample). According to the relation between the flare ribbon reconnection flux and the peak X-ray flux (Equation 4 and Figure 4), a flare of GOES class \sim X100 could be powered.

Our results are interesting in two aspects: for the solar case, as it means that for the strongest space weather effects (which are predominantly due to the CME rather than the flare), we can not simply extrapolate that the space weather effects will be increasingly stronger for flares produced by large ARs present on the Sun. Second, it has implications for the stellar case: we may speculate that in case of the much larger ARs (stellar spots) that are needed to produce the reported “superflares” on solar-type stars, the flares are probably mostly confined, as they will be associated with a very strong overlying AR strapping field. This may provide an explanation why the detection of stellar CMEs is rare (Drake et al. 2013; Odert et al. 2017; Moschou et al. 2019; Argiroffi et al. 2019), and implies that the solar-stellar connection between flare rates and CME rates may be fundamentally non-linear and actually “breaking” when we come to the very large events (Drake et al. 2013; Odert et al. 2017).

The confined flares from ARs with $\Phi_{AR} \geq 1.0 \times 10^{23}$ Mx are characterized by slipping reconnection, strong shear, and a stable filament. They belong to “type I” confined flares proposed by Li et al. (2019), who classified confined flares into two types based on their different dynamic properties and magnetic configurations. Similar to the appearance of confined flares in AR 12192 (Li et al. 2019), the filaments in ARs 11339, 11520 (Figures 6-7), 11967 and 12242 (Figures 8-9) were all stably present and seemed not to be involved in the flare evolution. The footpoints of high-temperature flare loops exhibited apparent slipping motions in both directions along flare ribbons (Figure 9), which implies the occurrence of slipping magnetic reconnection overlying the non-eruptive filaments (Li & Zhang 2015; Dudík et al. 2016; Lörinčík et al. 2019; Shen et al. 2019; Chen et al. 2019). We suggest that slipping flare loops along the two directions correspond to two different magnetic systems, and the continuous slipping magnetic reconnection between two magnetic systems causes the exchange of their magnetic connectivity and apparent bi-directional slipping motions of reconnecting field lines. Moreover, the PFLs observed in the gradual phase of the flares were strongly sheared, indicating a high non-potentiality. These observational characteristics of “type I” confined flares are inconsistent with the 2D standard CSHKP flare model (Carmichael 1964; Sturrock 1966; Hirayama 1974; Kopp & Pneuman 1976), which suggests that the reconnection is associated with the filament/flux rope eruption and occurs at a current sheet below the erupting filament. Our observations have revealed several different features. First, the filament/flux rope seemed to be neither disturbed nor erupting during or after the flare. Second, the reconnection site is more likely along the QSLs between two

magnetic systems overlying non-eruptive filaments. In summary, the signatures of “type I” confined flares in ARs with a large magnetic flux pose a challenge to the 2D classical flare model and need to establish 3D MHD models.

We thank the referee for helpful comments that improved the paper. We thank Xudong Sun for useful discussions. This work is supported by the National Natural Science Foundations of China (11533008, 11773039, 11903050, 11673035, 11790304, 11673034, 11873059 and 11790300), the National Key R&D Program of China (2019YFA0405000), the B-type Strategic Priority Program of the Chinese Academy of Sciences (XDB41000000), Key Programs of the Chinese Academy of Sciences (QYZDJ-SSW-SLH050), Young Elite Scientists Sponsorship Program by CAST (2018QNR001), the Youth Innovation Promotion Association of CAS (2014043 and 2017078) and NAOC Nebula Talents Program. Lijuan Liu was supported by NSFC (11803096) and the Open Project of CAS Key Laboratory of Geospace Environment. Astrid M. Veronig acknowledges the support by the Austrian Science Fund (FWF): P27292-N20. *SDO* is a mission of NASA’s Living With a Star Program, *STEREO* is the third mission in NASA’s Solar Terrestrial Probes Program, and *SOHO* is a mission of international cooperation between ESA and NASA.

REFERENCES

- Alissandrakis, C. E. 1981, *A&A*, 100, 197
- Amari, T., Canou, A., Aly, J.-J., Delyon, F., & Alauzet, F. 2018, *Nature*, 554, 211
- Andrews, M. D. 2003, *Sol. Phys.*, 218, 261
- Argiroffi, C., Reale, F., Drake, J. J., et al. 2019, *Nature Astronomy*, 3, 742
- Aulanier, G., Démoulin, P., Schrijver, C. J., et al. 2013, *A&A*, 549, A66
- Aulanier, G., Janvier, M., & Schmieder, B. 2012, *A&A*, 543, A110
- Aulanier, G., Pariat, E., Démoulin, P., & DeVore, C. R. 2006, *Sol. Phys.*, 238, 347
- Baumgartner, C., Thalmann, J. K., & Veronig, A. M. 2018, *ApJ*, 853, 105
- Bobra, M. G., Sun, X., Hoeksema, J. T., et al. 2014, *Sol. Phys.*, 289, 3549
- Bokenkamp, N. 2007, PhD thesis, Stanford Univ.
- Carmichael, H. 1964, *NASA Special Publication*, 50, 451

- Chen, A. Q., Wang, J. X., Li, J. W., et al. 2011, *A&A*, 534, A47
- Chen, H., Yang, J., Ji, K., et al. 2019, *ApJ*, 887, 118
- Chen, H., Zhang, J., Ma, S., et al. 2015, *ApJ*, 808, L24
- Cheng, X., Zhang, J., Ding, M. D., Guo, Y., & Su, J. T. 2011, *ApJ*, 732, 87
- Démoulin, P., Priest, E. R., & Lonie, D. P. 1996, *J. Geophys. Res.*, 101, 7631
- Drake, J. J., Cohen, O., Yashiro, S., et al. 2013, *ApJ*, 764, 170
- Duan, A., Jiang, C., He, W., et al. 2019, *ApJ*, 884, 73
- Dudík, J., Polito, V., Janvier, M., et al. 2016, *ApJ*, 823, 41
- Falconer, D. A., Moore, R. L., & Gary, G. A. 2002, *ApJ*, 569, 1016
- Fan, Y., & Gibson, S. E. 2007, *ApJ*, 668, 1232
- Forbes, T. G. 2000, *J. Geophys. Res.*, 105, 23153
- Gopalswamy, N., Yashiro, S., Michalek, G., et al. 2009, *Earth Moon and Planets*, 104, 295
- Gosling, J. T., McComas, D. J., Phillips, J. L., et al. 1991, *J. Geophys. Res.*, 96, 7831
- Green, L. M., Matthews, S. A., van Driel-Gesztelyi, L., Harra, L. K., & Culhane, J. L. 2002, *Sol. Phys.*, 205, 325
- Green, L. M., Török, T., Vršnak, B., et al. 2018, *Space Sci. Rev.*, 214, 46
- Guo, Y., Ding, M. D., Schmieder, B., et al. 2010, *ApJ*, 725, L38
- Hagyard, M. J., & Rabin, D. M. 1986, *Advances in Space Research*, 6, 7
- Hirayama, T. 1974, *Sol. Phys.*, 34, 323
- Howard, R. A., Moses, J. D., Vourlidas, A., et al. 2008, *Space Sci. Rev.*, 136, 67
- Jing, J., Liu, C., Lee, J., et al. 2018, *ApJ*, 864, 138
- Kaiser, M. L., Kucera, T. A., Davila, J. M., et al. 2008, *Space Sci. Rev.*, 136, 5
- Kazachenko, M. D., Lynch, B. J., Welsch, B. T., et al. 2017, *ApJ*, 845, 49
- Khodachenko, M. L., Ribas, I., Lammer, H., et al. 2007, *Astrobiology*, 7, 167

- Kliem, B., & Török, T. 2006, *Phys. Rev. Lett.*, 96, 255002
- Kopp, R. A., & Pneuman, G. W. 1976, *Sol. Phys.*, 50, 85
- Lammer, H., Lichtenegger, H. I. M., Kulikov, Y. N., et al. 2007, *Astrobiology*, 7, 185
- Lemen, J. R., Title, A. M., Akin, D. J., et al. 2012, *Sol. Phys.*, 275, 17
- Li, T., Liu, L., Hou, Y., et al. 2019, *ApJ*, 881, 151
- Li, T., & Zhang, J. 2015, *ApJ*, 804, L8
- Liu, L., Wang, Y., Wang, J., et al. 2016a, *ApJ*, 826, 119
- Liu, L., Wang, Y., Zhou, Z., et al. 2018, *ApJ*, 858, 121
- Liu, R., Kliem, B., Titov, V. S., et al. 2016b, *ApJ*, 818, 148
- Lörinčík, J., Dudík, J., & Aulanier, G. 2019, *ApJ*, 885, 83
- Lynch, B. J., Airapetian, V. S., DeVore, C. R., et al. 2019, *ApJ*, 880, 97
- Maehara, H., Shibayama, T., Notsu, S., et al. 2012, *Nature*, 485, 478
- Moore, R. L., Sterling, A. C., Hudson, H. S., et al. 2001, *ApJ*, 552, 833
- Morgan, H., & Druckmüller, M. 2014, *Sol. Phys.*, 289, 2945
- Moschou, S.-P., Drake, J. J., Cohen, O., et al. 2019, *ApJ*, 877, 105
- Nindos, A., & Andrews, M. D. 2004, *ApJ*, 616, L175
- Odert, P., Leitzinger, M., Hanslmeier, A., et al. 2017, *MNRAS*, 472, 876
- Pesnell, W. D., Thompson, B. J., & Chamberlin, P. C. 2012, *Sol. Phys.*, 275, 3
- Priest, E. R., & Démoulin, P. 1995, *J. Geophys. Res.*, 100, 23443
- Priest, E., & Forbes, T. 2000, *Magnetic Reconnection*
- Sarkar, R., & Srivastava, N. 2018, *Sol. Phys.*, 293, 16
- Scherrer, P. H., Schou, J., Bush, R. I., et al. 2012, *Sol. Phys.*, 275, 207
- Schrijver, C. J., Beer, J., Baltensperger, U., et al. 2012, *Journal of Geophysical Research (Space Physics)*, 117, A08103

- Shen, Y., Qu, Z., Zhou, C., et al. 2019, *ApJ*, 885, L11
- Shibata, K., Isobe, H., Hillier, A., et al. 2013, *PASJ*, 65, 49
- Shibata, K., & Magara, T. 2011, *Living Reviews in Solar Physics*, 8, 6
- Sturrock, P. A. 1966, *Nature*, 211, 695
- Su, Y., Golub, L., & Van Ballegoijen, A. A. 2007, *ApJ*, 655, 606
- Su, Y., Veronig, A. M., Holman, G. D., et al. 2013, *Nature Physics*, 9, 489
- Sun, X. 2013, arXiv e-prints, arXiv:1309.2392
- Sun, X., Bobra, M. G., Hoeksema, J. T., et al. 2015, *ApJ*, 804, L28
- Svestka, Z. 1986, *The Lower Atmosphere of Solar Flares*, 332
- Thalmann, J. K., Su, Y., Temmer, M., et al. 2015, *ApJ*, 801, L23
- Titov, V. S., Hornig, G., & Démoulin, P. 2002, *Journal of Geophysical Research (Space Physics)*, 107, 1164
- Toriumi, S., Schrijver, C. J., Harra, L. K., et al. 2017, *ApJ*, 834, 56
- Tschernitz, J., Veronig, A. M., Thalmann, J. K., et al. 2018, *ApJ*, 853, 41
- Vasantharaju, N., Vemareddy, P., Ravindra, B., et al. 2018, *ApJ*, 860, 58
- Veronig, A. M., & Polanec, W. 2015, *Sol. Phys.*, 290, 2923
- Wang, Y., & Zhang, J. 2007, *ApJ*, 665, 1428
- Wheatland, M. S., Sturrock, P. A., & Roumeliotis, G. 2000, *ApJ*, 540, 1150
- Wiegmann, T. 2004, *Sol. Phys.*, 219, 87
- Yang, S., Zhang, J., & Xiang, Y. 2014, *ApJ*, 793, L28
- Yashiro, S., Akiyama, S., Gopalswamy, N., et al. 2006, *ApJ*, 650, L143
- Zhang, J., Wang, Y., & Liu, Y. 2010, *ApJ*, 723, 1006
- Zuccarello, F. P., Aulanier, G., & Gilchrist, S. A. 2015, *ApJ*, 814, 126

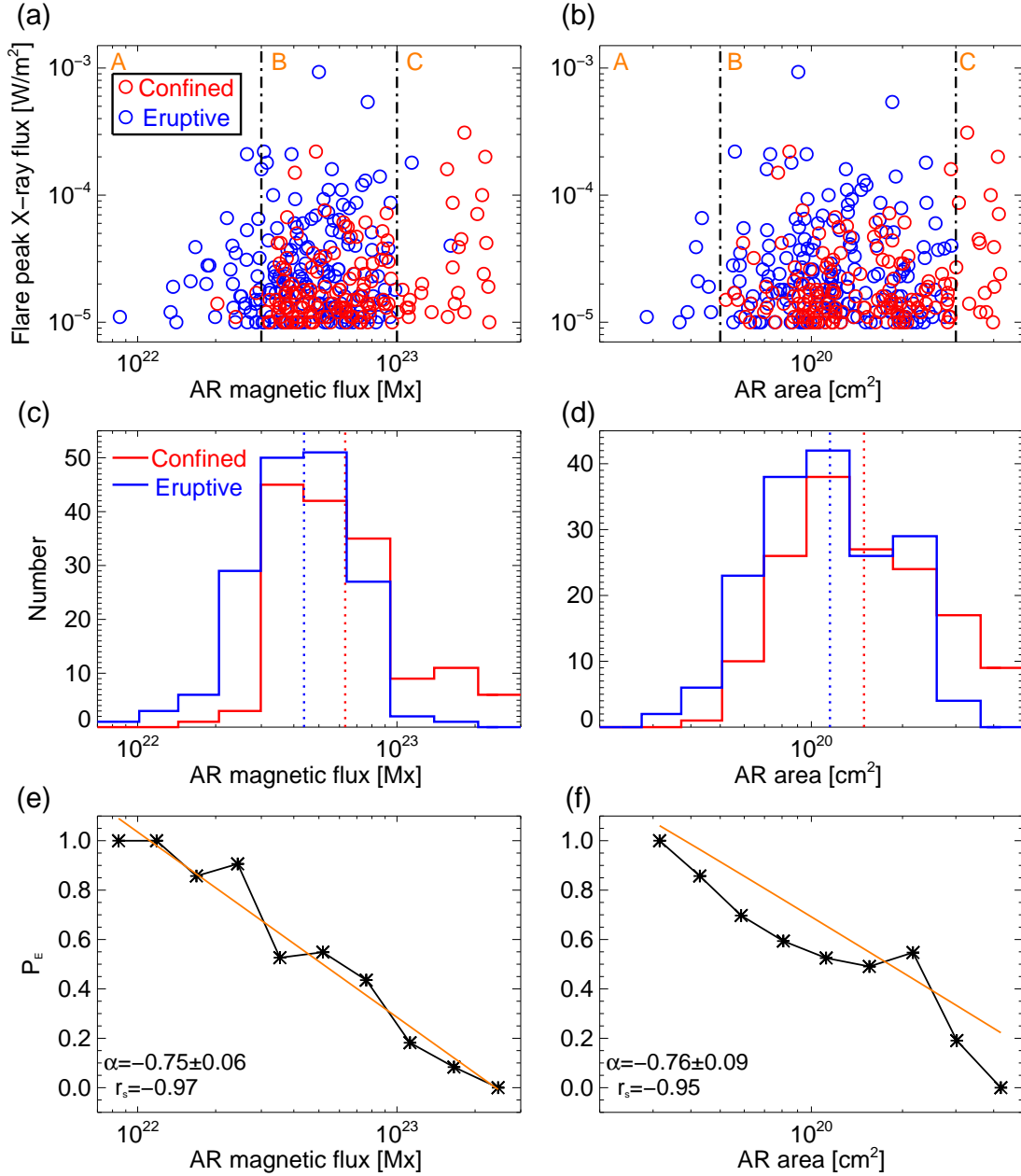


Fig. 1.— Relations of the eruptive character of large solar flares with unsigned AR magnetic flux and AR area. Top: scatter plots of flare peak X-ray flux vs. unsigned AR magnetic flux and AR area. Blue (red) circles are the eruptive (confined) flares. Two vertical dash-dotted lines in panel (a) respectively refer to AR magnetic flux of 3.0×10^{22} Mx and 1.0×10^{23} Mx. Two vertical dash-dotted lines in panel (b) respectively correspond to AR area of 5.0×10^{19} cm^2 and 3.0×10^{20} cm^2 . Middle: histograms of AR magnetic flux and AR area for confined (red) and eruptive (blue) events. Dotted vertical lines indicate the means of the log values. Bottom: proportions of eruptive flares P_E vs. unsigned AR magnetic flux and AR area. Orange lines show the results of linear fitting, and slopes α and Spearman rank order correlation coefficients r_s are shown at the bottom left.

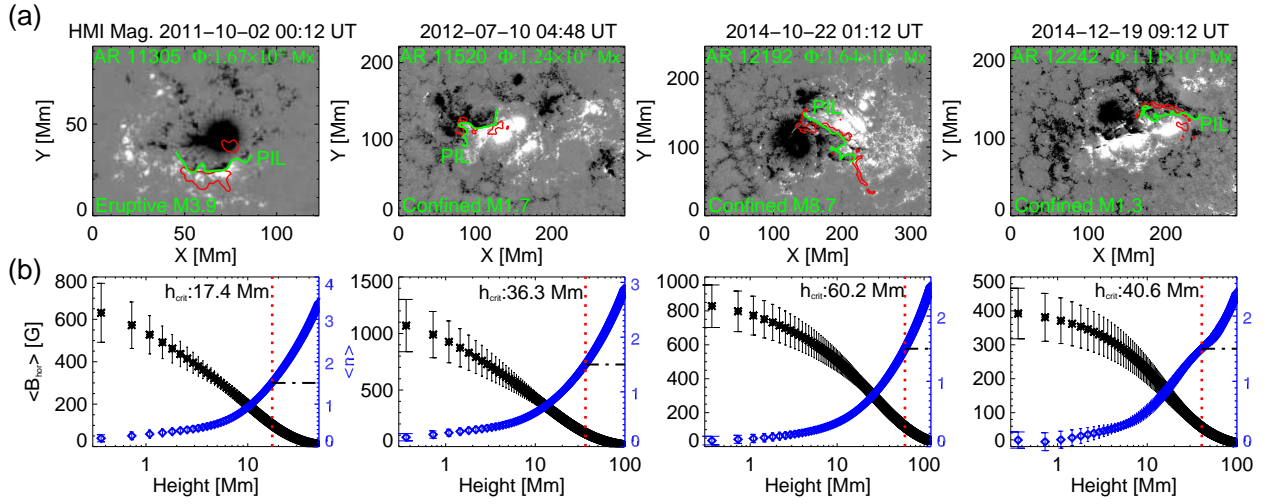


Fig. 2.— Decay index of the coronal background fields for four examples. (a) SDO/HMI photospheric magnetograms B_n with contours of the AIA 1600 Å flare ribbon brightenings (red contours) overplotted. From left to right: eruptive M3.9-class flare in AR 11305, confined flares of class M1.7 in AR 11520, M8.7 in AR 12192 and M1.3 in AR 12242. Green curves denote the flare-relevant PILs along which the mean decay index is calculated. (b) $\langle B_{hor} \rangle$ (black asterisks) and $\langle n \rangle$ (blue diamonds) as a function of height. The error bars mark the corresponding standard deviation. Horizontal black lines denote the position where $\langle n \rangle$ equals 1.5 and red vertical lines correspond to the critical height h_{crit} for each event.

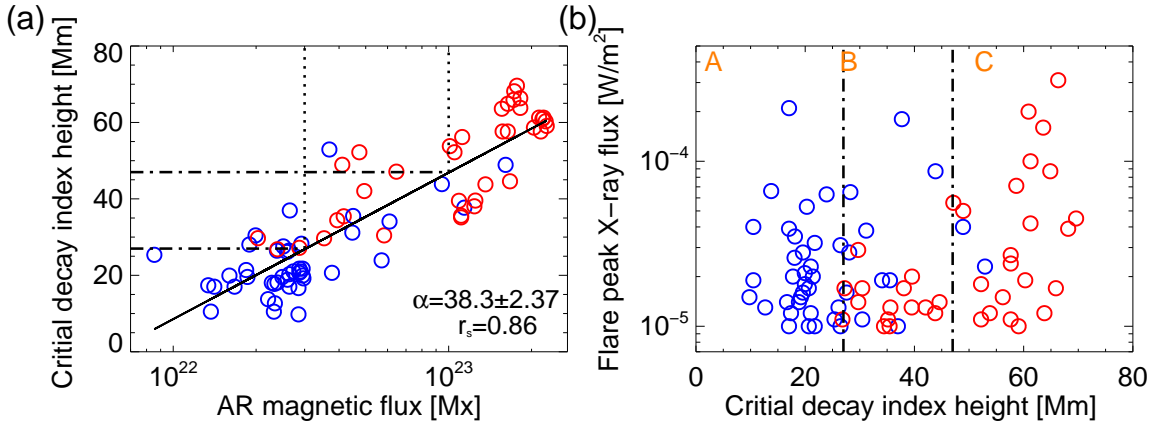


Fig. 3.— Scatter plots of critical decay index height vs. unsigned AR magnetic flux and flare peak X-ray flux vs. critical decay index height. Blue (red) circles are the eruptive (confined) flares. The black solid line in panel (a) shows the result of a linear fitting, and slope α and Spearman rank order correlation coefficients r_s are shown at the bottom right. Two vertical dotted lines in panel (a) denote the positions where Φ_{AR} respectively equals 3.0×10^{22} Mx and 1.0×10^{23} Mx. Two horizontal dash-dotted lines in panel (a) and two vertical dash-dotted lines in panel (b) respectively refer to critical decay index height of 27 Mm and 47 Mm.

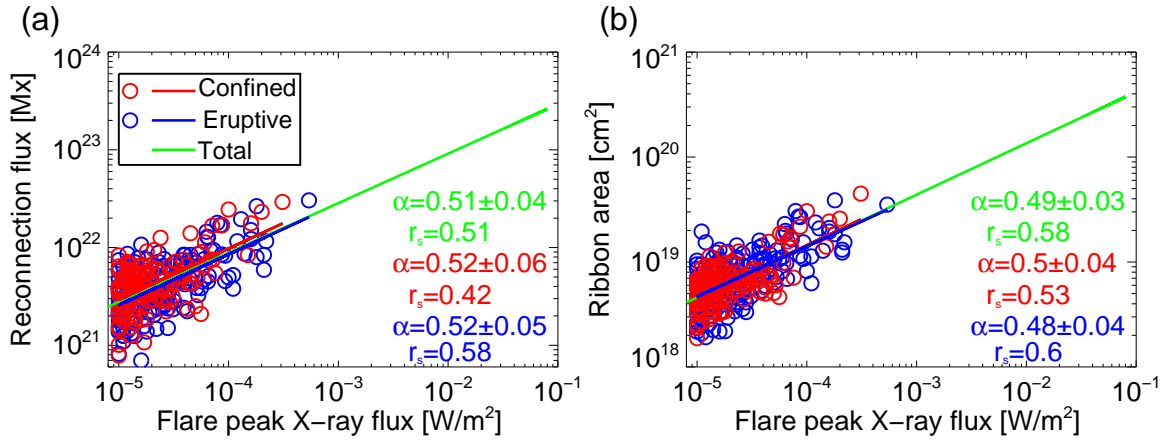


Fig. 4.— Scatter plots of unsigned flare reconnection magnetic flux and ribbon area vs. flare peak X-ray flux for confined (red) and eruptive (blue) flares. Red, blue and green straight lines show the results of linear fitting respectively for confined, eruptive and total events. The slopes α and Spearman rank order correlation coefficients r_s are shown at the bottom right.

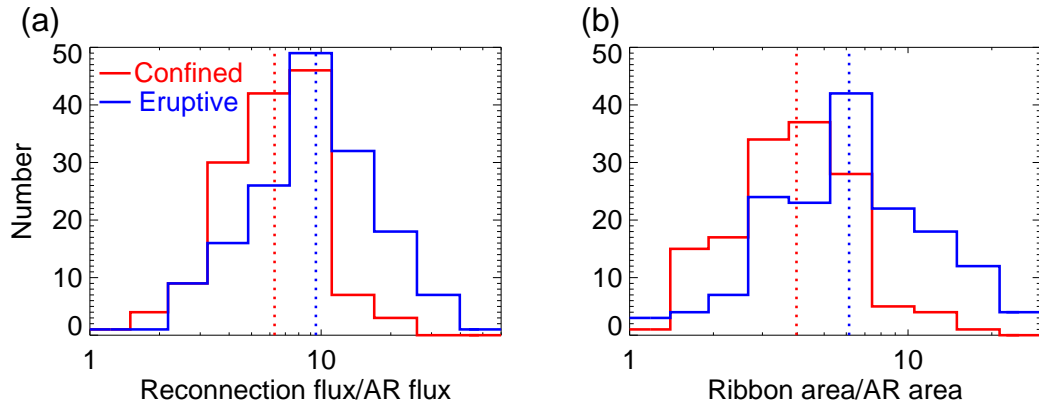


Fig. 5.— Histograms of the ratios of flare reconnection flux/AR flux and ribbon area/AR area for confined (red) and eruptive (blue) events. Dotted vertical lines indicate the means of the log values.

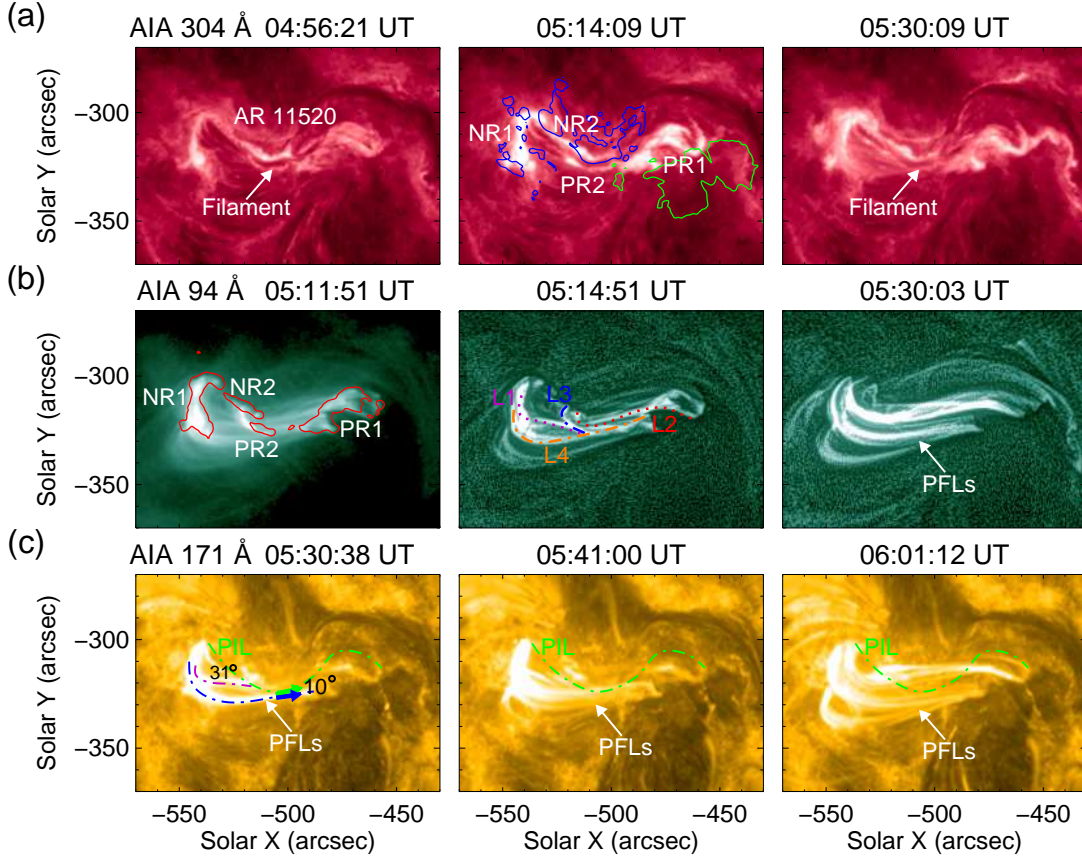


Fig. 6.— Appearance of the confined M1.7-class flare in AR 11520 on 10 July 2012. (a) SDO/AIA 304 Å images showing the stable filament before and after the flare. Green and blue contours are the LOS magnetic fields at ± 750 G levels. PR1-PR2 are two positive-polarity flare ribbons and NR1-NR2 are two negative-polarity ribbons. (b) AIA 94 Å images displaying the dynamic evolution of high-temperature flare loops. Red contours denote the AIA 1600 Å flare brightenings. L1-L4 outline four sets of loop bundles and white arrow points to sheared post-flare loops. (c) AIA 171 Å images showing the low-temperature PFLs. Two sets of PFLs (purple and blue dashed-dotted curves) are delineated to estimate their inclination angles with respect to the PIL (green dash-dotted line). The animation of this figure includes AIA 304, 171 and 94 Å images from 04:58 UT to 05:41 UT. The video duration is 3 s.

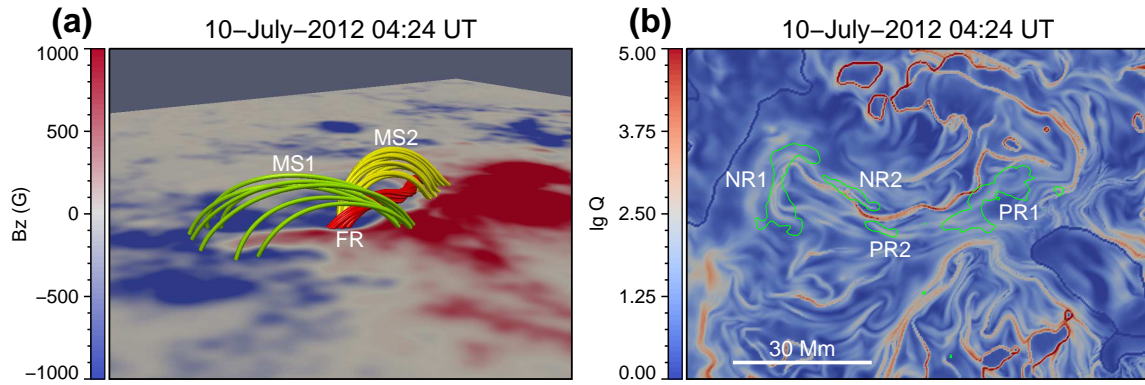


Fig. 7.— Magnetic field configuration of the flare region. (a) Side view of extrapolated field lines showing two magnetic systems MS1-MS2 and the underlying flux rope FR. (b) Map of the squashing factor Q on the HMI bottom boundary calculated from the nonlinear force-free field. Green contours outline the flare ribbon brightenings in the AIA 1600 Å channel.

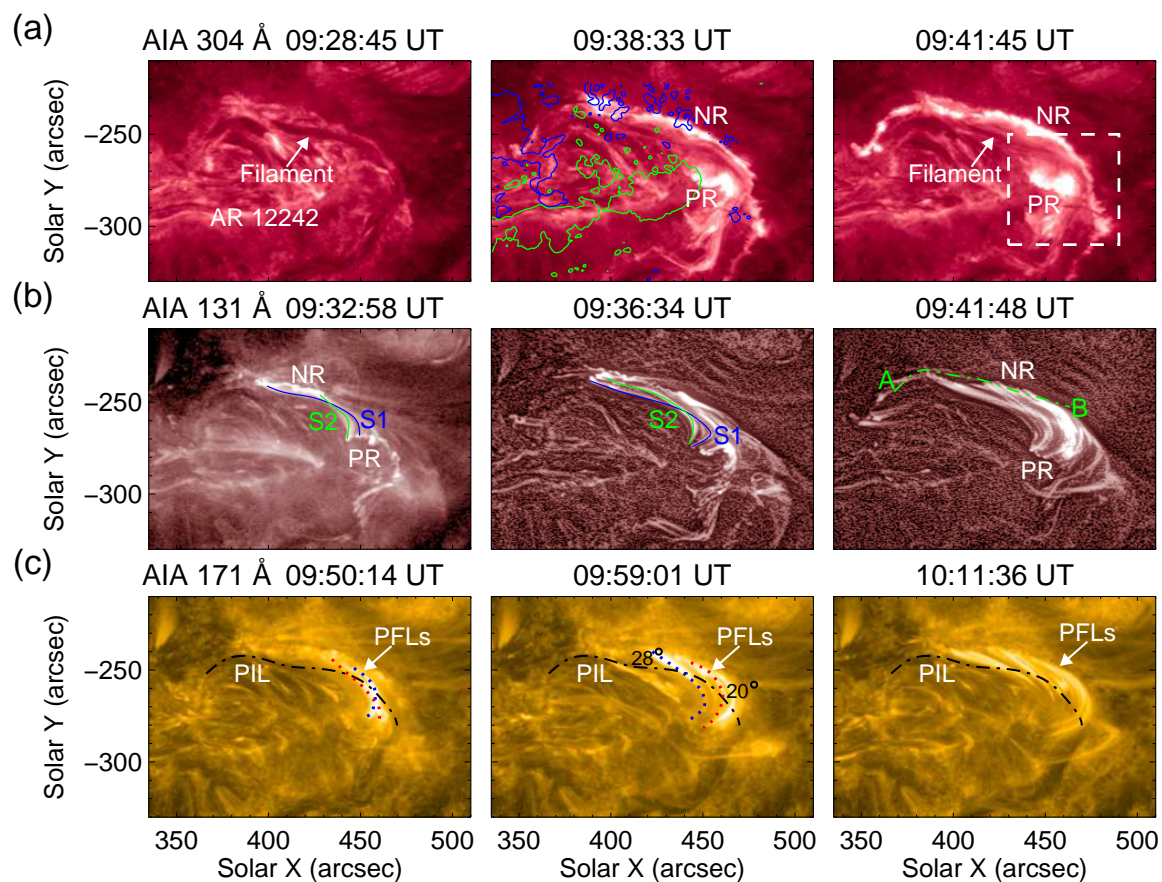


Fig. 8.— Appearance of the confined M1.3-class flare in AR 12242 on 19 December 2014. (a) SDO/AIA 304 Å images showing the non-eruptive filament throughout the flare. Green and blue contours are the HMI LOS magnetic fields at ± 350 G levels. NR and PR are two quasi-parallel flare ribbons. The white square denotes the field of view (FOV) of Figure 9. (b) AIA 131 Å images displaying two magnetic systems S1 and S2. Green dash-dotted curve “A-B” shows the cut position used to obtain the stack plot shown in Figure 9. (c) AIA 171 Å images showing the low-temperature PFLs. Red and blue dotted curves outline the PFLs at different times and the black dash-dotted line delineates the PIL associated with the flare. The animation of this figure includes AIA 304, 171 and 131 Å images from 09:25 UT to 10:11 UT. The video duration is 3 s.

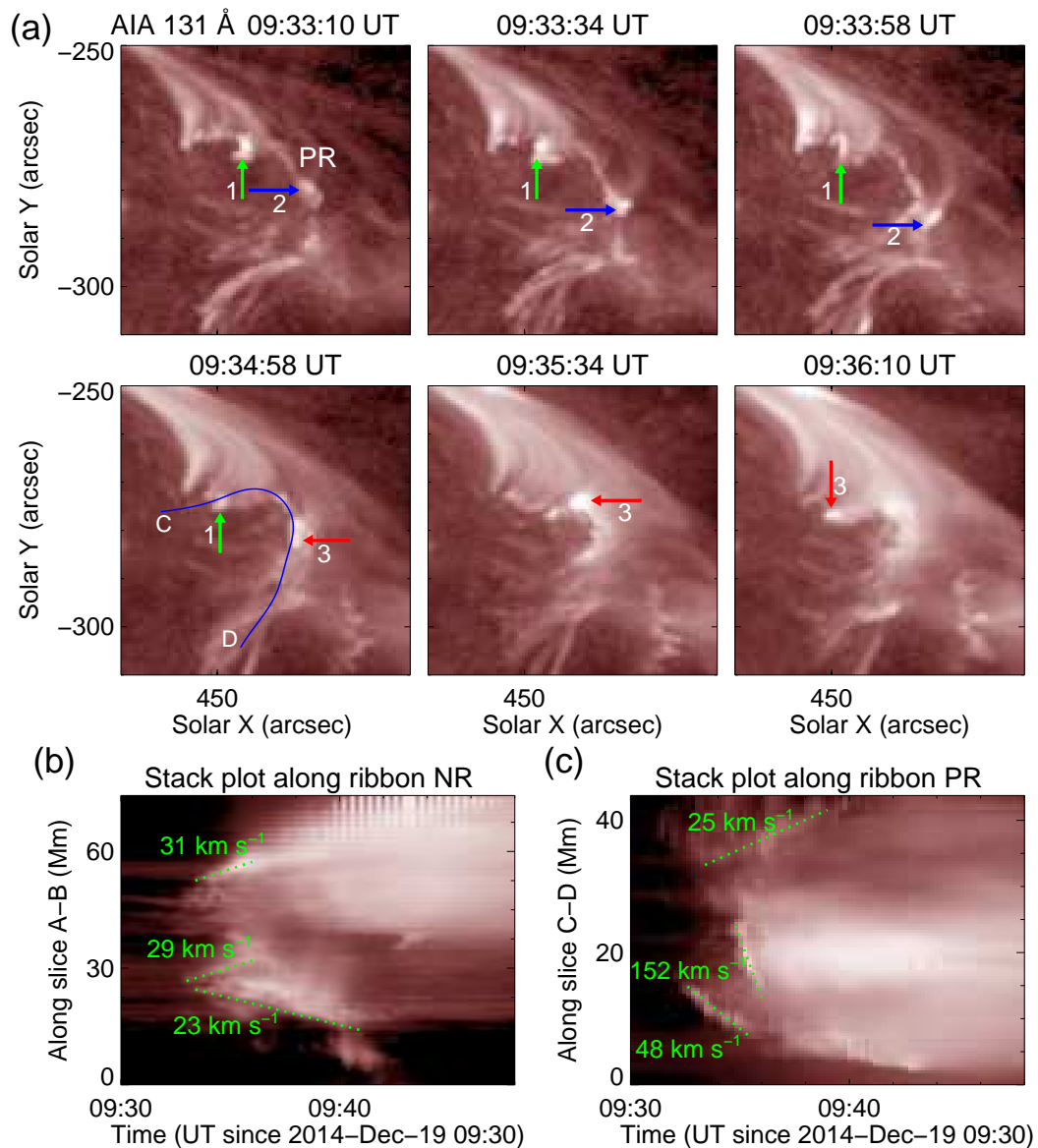


Fig. 9.— Apparent slipping motions of fine structures within flare ribbons PR and NR. (a) Time series of SDO/AIA 131 Å images showing the slippage of traced bright knots (“1” – “3”) within ribbon PR. Bright knots “1” and “3” slipped toward the east end of PR and knot “2” slipped in the opposite direction. The blue curve “C–D” shows the cut position used to obtain the stack plot shown in panel (c). (b)–(c) 131 Å stack plots along slices “A–B” and “C–D” showing the bidirectional slippage along ribbons NR and PR.

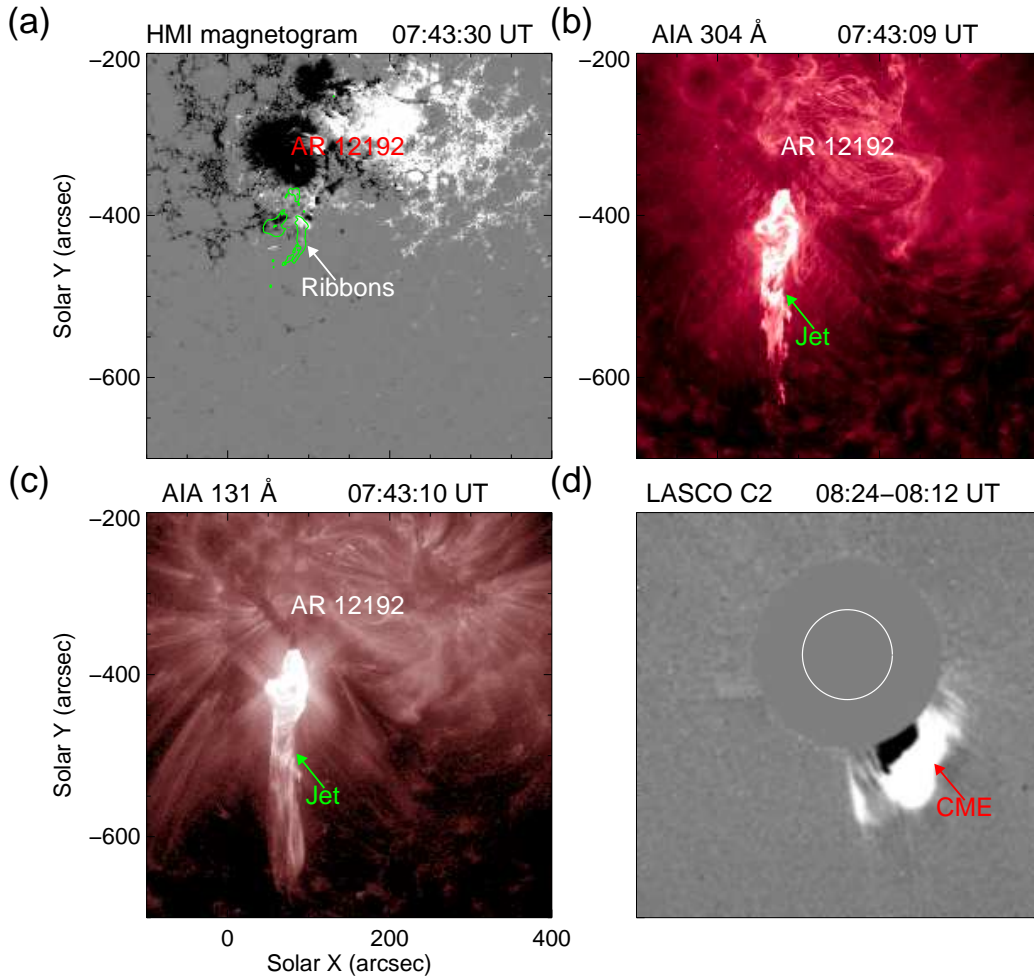


Fig. 10.— Appearance of the eruptive M4.0-class flare in AR 12192 on 24 October 2014. (a) SDO/HMI LOS magnetogram with contours of the AIA 1600 Å flare brightenings (green contours) overplotted. (b)-(c) AIA 304 and 131 Å images displaying the blow-out jet at the southeast edge of AR 12192. (d) LASCO/C2 running-difference image showing the associated CME.

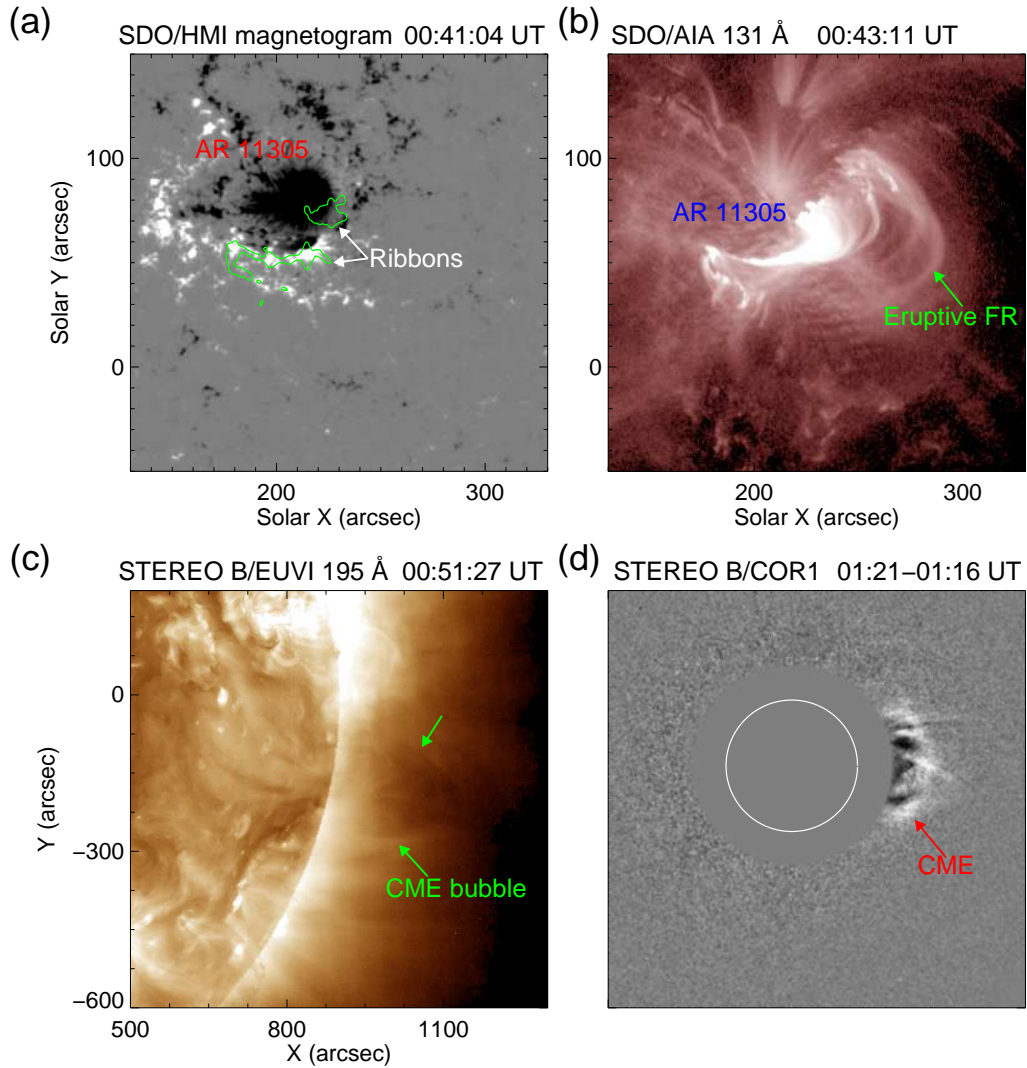


Fig. 11.— Overview of the eruptive M3.9 flare on 02 October 2011 in AR 11305. (a) SDO/HMI LOS magnetogram with contours of the AIA 1600 Å flare brightenings (green contours) overplotted. (b) AIA 131 Å image displaying the eruptive flux rope. (c) STEREO B/EUVI 195 Å image showing the generated CME bubble. (d) STEREO B/COR1 image displaying the associated CME.

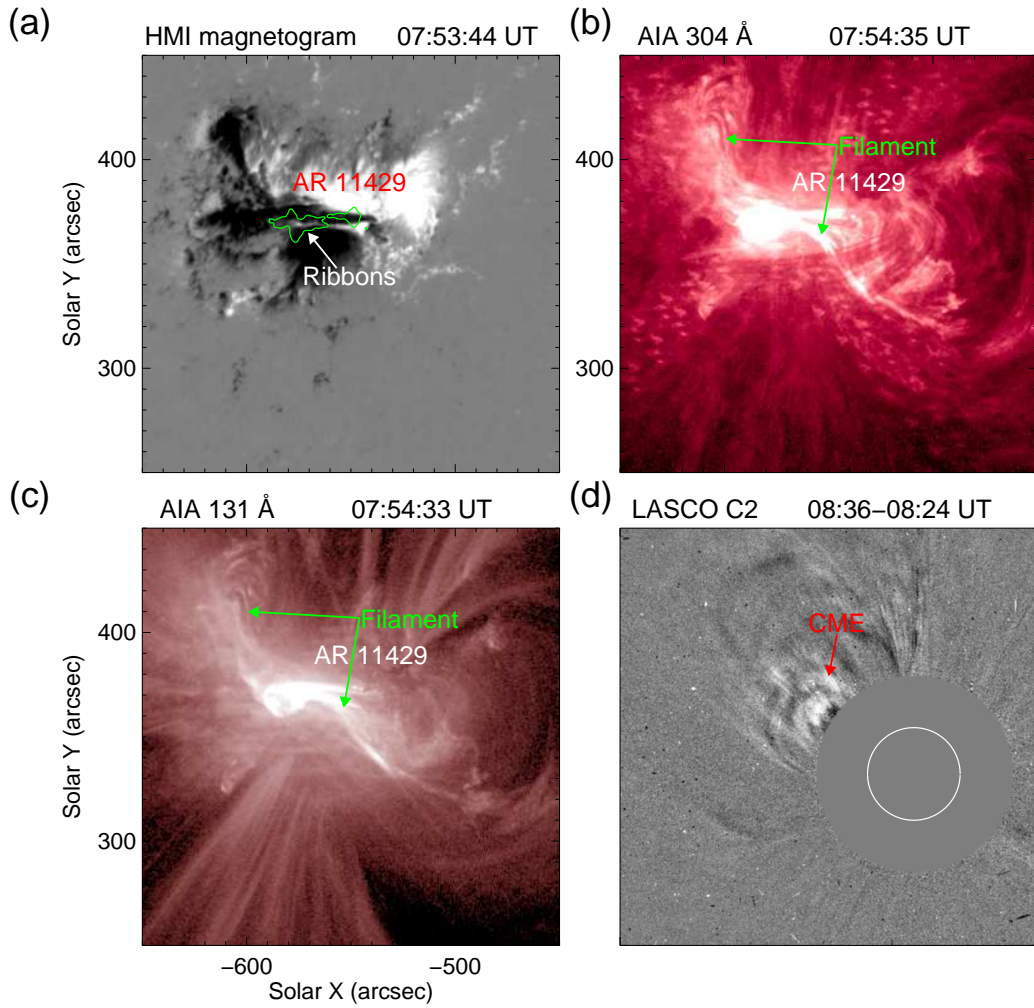


Fig. 12.— Appearance of the eruptive M1.0-class flare in AR 11429 on 06 March 2012. (a) SDO/HMI LOS magnetogram with contours of the AIA 1600 Å flare brightenings (green contours) overplotted. (b)-(c) AIA 304 and 131 Å images displaying the partial-eruptive filament. (d) LASCO/C2 running-difference image showing the associated CME.

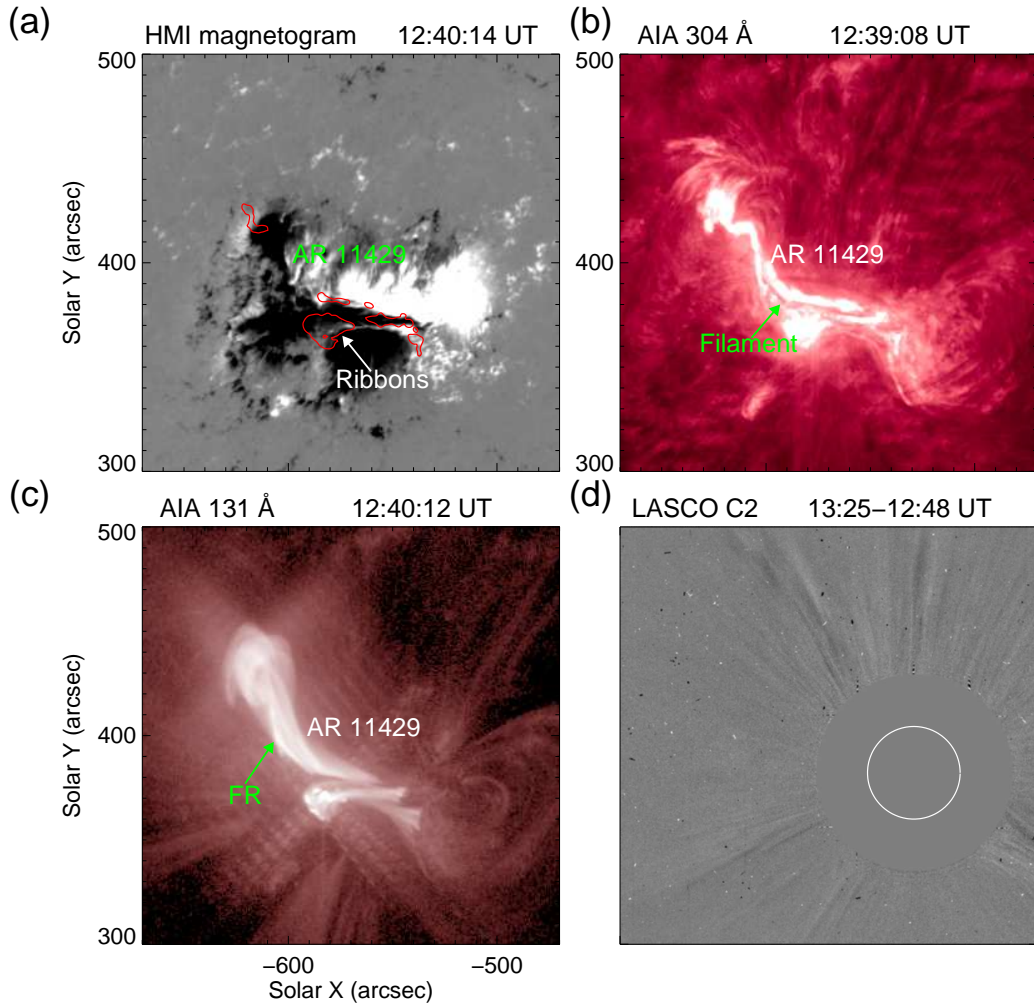


Fig. 13.— Appearance of the confined M2.1-class flare in AR 11429 on 06 March 2012. (a) SDO/HMI LOS magnetogram with contours of the AIA 1600 Å flare brightenings (red contours) overplotted. (b) AIA 304 Å image displaying the non-eruptive filament along the PIL. (c) AIA 131 Å image showing the failed eruption of the flux rope. (d) LASCO/C2 running-difference image.